Subproject C4.5

Electron Microscopy Studies of the Properties of Nanoparticles and Nanostructured Materials

Principle Investigator: Dagmar Gerthsen

CFN-Financed Scientists: Radian Popescu (BAT IIa, 48 months)

Further Scientists: Dr. habil. Reinhard Schneider, Eric Prestat (Diplom student)

Laboratorium für Elektronenmikroskopie
Universität Karlsruhe (TH)

Electron Microscopy Studies of the Properties of Nanoparticles and Nanostructured Materials

1. Introduction and Summary

Nanoscaled metal clusters deposited on different substrates have been intensively studied in the past due to their unique properties as compared to the corresponding bulk materials. They exhibit a wide range of properties of fundamental and technological significance, like, for example: a) a stability pattern at certain sizes corresponding to the structural shell-filling "magic numbers", b) quasicrystalline structures, which have near-ideal strength, c) specific transport, optical, and chemical properties related to their electronic structure. However, not only structure and properties of deposited clusters are interesting for applications. The dynamics and stability of nanoclusters on substrates can be also of crucial importance for many issues in surface science in context with the strong dependence of physical and chemical properties of clusters on the cluster size. For example, the negative temperature coefficient of the electrical resistivity, optical transmission coefficient, and superparamagnetic susceptibility, all strongly depend on the cluster size and their separation on the substrate. Moreover, a gradual decay of the catalytic activity with increasing cluster sizes is often observed, which can be attributed to the decreasing of surface/core-atom ratio.

Systems composed of Au and Pt clusters on different substrates are important as industrial catalysts. It was shown, for example, that Au clusters with sizes between 2 and 3 nm exhibit an exceptional catalytic activity in CO-oxidation reactions, while Pt clusters show a high catalytic activity for hydrogen-dissociation and hydrogen-oxidation at low temperature. Furthermore, Pt clusters deposited on carbon materials are important as electrocatalysts in proton-exchange membrane fuel cells and Au clusters are relevant as prototype material for nanoscaled electronic devices and biosensors. All these applications have motivated numerous studies regarding the properties of Au and Pt clusters and their dynamics on particular support materials.

In the following short summaries are given of published work of project C4.5. The report will focus of work on Pt clusters and novel nanoparticles in chapters 2 to 4.

According to the large interest paid to the Au clusters, the basic properties of Au clusters supported on amorphous carbon (a-C) substrates were investigated. One of the fundamental material properties is the mean inner Coulomb potential (MIP), which can be defined as the volume-averaged electrostatic part of the crystal potential. The MIP plays an important role for the quantitative evaluation of experimental data obtained from electron scattering techniques like transmission electron microscopy (TEM), electron holography (EH) and low-energy electron diffraction. We studied the MIP of nanoscaled Au clusters by using off-axis EH [1]. A strong increase of the mean inner potential is observed for Au clusters from 30 V for bulk gold up to 80 V for clusters with a radius of 0.5 nm. The rapid increase of the Au MIP with decreasing cluster size is explained by the shortening of the bond lengths between surface and core atoms of the cluster which leads to an increase of the electron density. The increase of the MIP has serious consequences for the quantification of electron scattering data because the mean inner potential determines the amplitude of the electron wave scattered in forward direction. For small Au clusters the electron wave scattered in forward direction is significantly stronger compared to bulk gold.

Besides fundamental research application-relevant studies were performed. For example, the stability of cluster-size distributions and immobilization of clusters on amorphous carbon (a-C) substrates were investigated. Coarsening of cluster-size distributions will typically occur by Ostwald ripening (OR) and/or Smoluchowski ripening (SR) (coalescence of mobile clusters due to Brownian motion). Coarsening is technologically important, e.g. with respect to the efficiency of catalysts, which requires nanoparticles within a small size interval. Using TEM, room-temperature coarsening of mass-selected Au_n (n = 4, 6, 13 and 20) clusters produced in the group of M.M. Kappes (project C.4.6) was investigated [2]. The clusters are deposited on amorphous carbon (a-C) substrates, where strong bonding of small clusters on the substrate occurs and the suppression of SR. Despite cluster immobilization, a significant increase of the average cluster radius $\overline{R}$ with time is observed even at room temperature due to surface OR. Moreover, the detailed analysis of the surface-mass-transport diffusion coefficients suggests that the rate of the surface OR for mass-selected Au_n clusters increases with the cluster size in the sequence: $Au_4 \approx Au_6 < Au_{13} < Au_{20}$ for the investigated range of Au clusters [2]. Analogous studies were carried out for Pt clusters [3] which are described in chapter 3 of this report.

Within the frame of fundamental research performed in project C4.5, high-resolution (HR) TEM was applied to image single Pt atoms in an aberration-corrected transmission electron microscope [4]. Single atoms are the most basic objects for TEM imaging which facilitates testing of concepts for image-contrast modeling. Full agreement on an absolute intensity scale is obtained between experimental and simulated single-atom contrast of isolated Pt atoms. More details will be presented in chapter 2 of this report.

Another task of project C4.5 is the investigation of novel nanoparticles prepared in the group of C. Feldmann (Project C1.4). High-resolution (HR) TEM is particularly important for the study of hollow nanoparticles to measure the cavity size and wall thickness [5-9]. In addition, a methodical study was carried out which compares the diameters of massive and hollow nanoparticles derived from different techniques (HRTEM, X-ray diffraction, dynamic light scattering and differential sedimentation). Formalisms for the evaluation of X-ray diffraction (XRD) data are available to derive the average size and strain for an ensemble of massive nanoparticles. However, these formalisms fail for hollow particles. Based on structural data from several different techniques we have developed an XRD evaluation formalism [10] which yields the average outer and inner diameter of hollow nanoparticle ensembles (see chapter 4 of this report).

2. Quantitative HRTEM on single Pt atoms

In context with the study of Pt clusters we have carried out a fundamental study on quantitative HRTEM imaging of single Pt atoms. Single atoms can be considered as the most basic objects in electron microscopy. From an electron-optical point of view, imaging of single atoms is clearly feasible after the introduction of correction lens systems for spherical and other aberrations up to the fifth order (for short Cs-corrector) which have improved spatial resolution up to 50 pm [11]. Numerous studies are already published which are concerned with HRTEM imaging of single atoms and corresponding image simulations. However, a comparison between simulated and experimental single-atom images ***on an absolute intensity scale*** has never been presented. Analyses on an absolute intensity scale are absolutely necessary to assess quantitatively e.g. differential scattering cross-sections of single atoms and the validity of modelling the imaging process in the microscope.

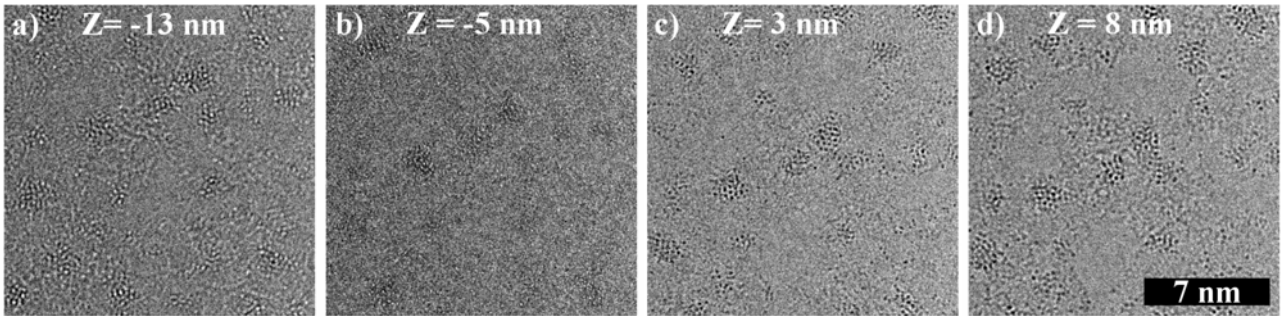

FIG. 1. Experimental HRTEM images of single Pt atoms and small clusters of Pt atoms on SAM recorded at different defocus values Z as indicated for a)-d).

Imaging single atoms by HRTEM is based on phase contrast, where the interaction between electron wave and atom only induces a phase shift with negligible amplitude change of the scattered electron wave. This leads to weak single-atom contrast which depends strongly on the transfer characteristics of the microscope determined by defocus and other lens aberrations. Due to the strong dependence on the imaging conditions, HRTEM images can in general not be interpreted intuitively. Instead, series of images of the same object region taken with different defocus values (denoted as through-focal series) are usually required to extract quantitative information from HRTEM images. Another prerequisite for quantitative single-atom imaging is a sufficiently thin supporting substrate which does not modify significantly the vacuum image intensity. A promising type of substrate are self-assembled monolayer (SAM) films consisting of 1,1'-biphenyl-4-thiol molecules cross-linked by electron irradiation with a thickness of ≈1.6 nm [12].

The investigated sample was prepared by electron-beam evaporation of 0.2 monolayers Pt (1 monolayer: $1.3 \cdot 10^{15}$ atoms/cm^2) on a SAM substrate. A defocus series was recorded which consists of 36 single HRTEM images subsequently taken with a defocus step of 1 nm between -19 nm and +16 nm. Fig. 1 shows typical HRTEM images of small planar Pt clusters and isolated Pt atoms on SAM at different defocus values Z as indicated on the images. Fig. 1(a) shows bright atom contrast under underfocus conditions. The intensity of the Pt-atom contrast vanishes almost completely in Fig. 1(b) at Z=-5 nm until the contrast reverses under overfocus conditions in Figs. 1(c,d). The background intensity associated with the SAM substrat e can hardly be distinguished from the vacuum intensity in small holes visible in Fig. 1(d). Intensity profiles of isolated atoms are obtained by averaging profiles along the horizontal and vertical image axis at several different defocus values. Fig. 2 shows a representative intensity profile at Z=-10 nm. A simulated profile is included in Fig. 2 which is in good agreement with the experimental profile considering the noise level of 3 %. For a quantitative comparison of experimental and simulated images, the maximum intensity normalized with respect to the background intensity and the full width half maximum (FWHM) of the intensity profiles were chosen. Another quantitative feature is the radius of the first side minimum/maximum (underfocus/overfocus images) of the fringe-like contrast around the central peak.

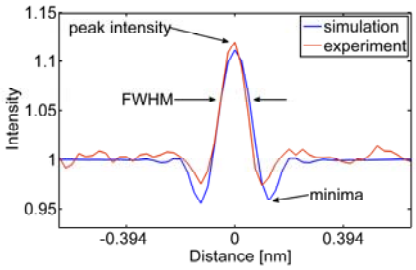

FIG. 2. Normalized intensity profile across a single Pt atom taken from an experimental (red) and simulated (blue) HRTEM image at an underfocus value of -10 nm.

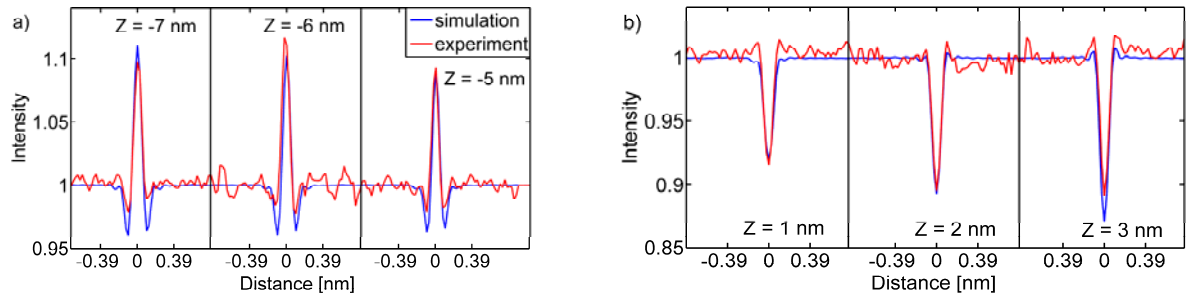

FIG. 4. Experimental (red) and simulated (blue) intensity profiles across single Pt atoms at a) underfocus values of -7 nm, -6 nm and -5 nm and b) overfocus values of 1 nm, 2 nm and 3 nm.

The imaging process is modeled by Fourier optics taking into account all known instrumental effects including wave aberrations, partial coherence and the modulation transfer function of the CCD camera. Weickenmeier-Kohl [13] and Doyle-Turner [14] differential scattering-cross sections were tested to describe the scattering behavior of single Pt atoms. Best agreement between simulated and experimental single-atom contrast is obtained for the Weickenmeier-Kohl differential scattering-cross sections. The quantitative agreement between simulation and experiment is demonstrated in Fig. 3, which shows six representative intensity profiles for three different underfocus (Fig. 3(a)) and three different overfocus values (Fig. 3(b)).

3. Coarsening of Pt clusters

It is generally accepted that possible technological applications of clusters are hampered by the lack of methods for cluster pinning at specific surface sites and the required high long-term stability of the cluster-size distribution. With respect to using Pt clusters as catalysts, the main problem is related to the progressive loss of active surface area due to cluster coarsening. This motivates our study of the stability and time evolution of the cluster-size distribution at different temperatures to determine the dominant coarsening mechanisms.

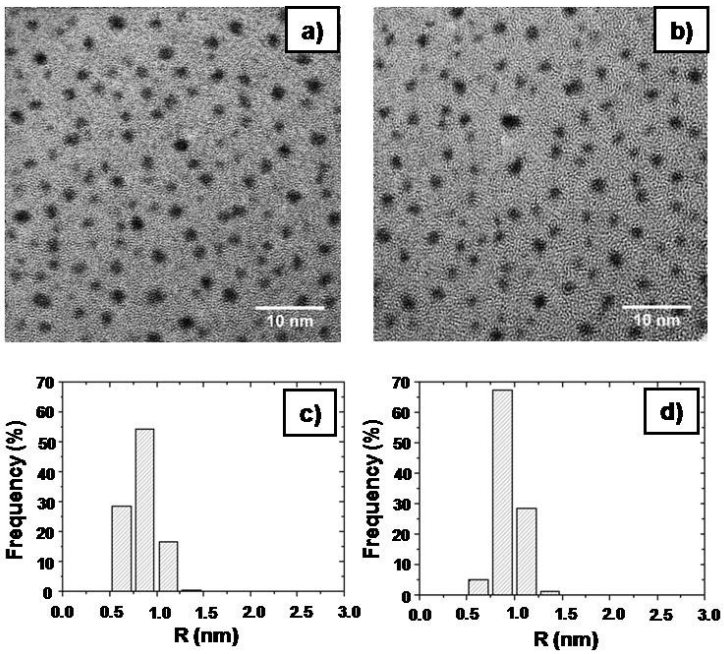

FIG. 4. Pt clusters on a-C substrate: TEM images recorded after 2 h (a) and 15 h (b) annealing at 200 °C; Histograms of cluster-radius distributions determined after 2 h (c) and 15 h (d) annealing at 200 °C.

Pt clusters were deposited on commercial amorphous carbon (a-C) thin films (10-12 nm thick) by electron-beam vapor deposition. The cluster-size distributions at 200, 225, 250 and 300 °C were investigated by TEM as a function of annealing time in regular time intervals. Between 150 and 300 Pt clusters were analyzed for each time interval. We assume circular cluster-projection areas in our analysis, which can be converted to cluster radii. Histograms of cluster radii yield the average cluster radii at a given time $\overline{R}(t)$. Fig. 4 shows TEM micrographs and the corresponding cluster-radius distributions measured after annealing at 200 °C for 2 and 15 h.

Fig. 5 shows the measured $\overline{R}(t)$ values which increase with annealing time. The coarsening kinetics of Pt clusters during the first 2 hours of annealing at 200, 225, 250 and 300 °C is fast and can be explained by significant redistribution of the deposited Pt clusters due to cluster coalescence (Smoluchowski ripening (SR)). *In-situ* annealing in a transmission electron microscope at 470 °C (Fig. 6) shows that, besides surface Ostwald ripening (OR), a very active coalescence of mobile Pt clusters takes place during the first 2 hours. The SR kinetics rapidly slows down with time for two reasons. First, the surface diffusion coefficients of Pt clusters decrease with increasing cluster sizes and, second, the average inter-cluster distance increases with decreasing cluster density on the substrate. This allows us to neglect SR within the second ripening stage, which sets in after about 2 h.

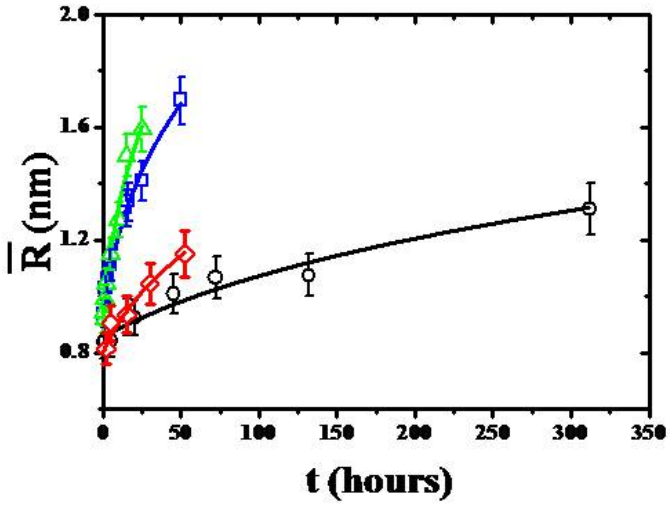

FIG. 5. Average radii of Pt clusters $\overline{R}(t)$ as a function of annealing time t at different temperatures: 200°C (○), 225°C (◇), 250°C (□) and 300°C (△). The solid lines of the corresponding color are the fit curves of the data for diffusion limited kinetics of surface OR.

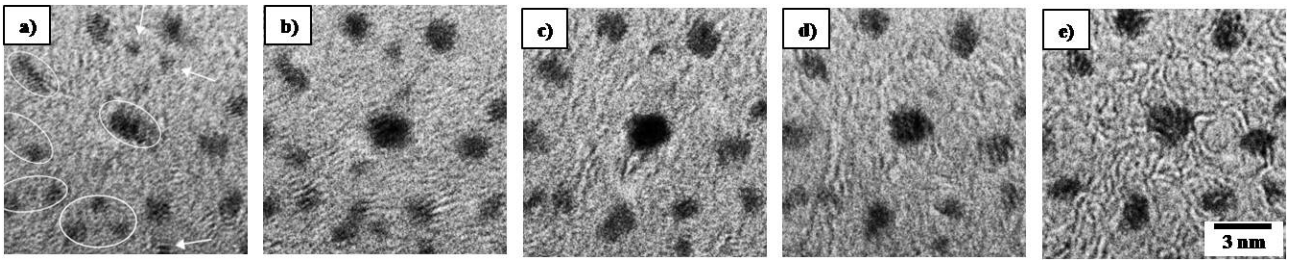

FIG. 6. In-situ TEM study of Pt-cluster coarsening: TEM images recoded after 0 h (a), 1 h (b), 2 h (c), 3 h (d) and 5.5 h (e) annealing at 470 °C. The circles are used to show Pt clusters which coarsen by SR, while arrows mark clusters which grow or decay by surface OR.

The coarsening process during the second ripening stage can be well described by a least-square fit of the experimental $\overline{R}(t)$ values based on the expression $\overline{R}^4(t) = \overline{R}^4(0) + K_d\, t$ (t: time, K_d: constant), which corresponds to surface diffusion-limited OR with the mass transport taking place through the cluster-substrate contact perimeter [15] (sold lines in Fig. 5). K_d depends on the temperature and can be derived from the fit curves in Fig. 5.

A quantitative description of the OR process can be obtained by comparing the surface-mass-transport diffusion coefficient D_s' values, because faster kinetics results in larger D_s' values. The D_s' values can be calculated using the K_d values and the relation $D_s' = \frac{45 \ln(L)\, \varphi(\theta)\, k_B\, T}{4\, \omega^2\, \gamma\, n_0} K_d$ [16] with the volume of Pt-atom $\omega = 1.51 \cdot 10^{-29}$ m^3, the Pt-surface energy $\gamma = 3.0$ Jm^{-2} [17], the Boltzmann constant k_B and the absolute temperature T. L=2.5 (in units of cluster radius) is the screening distance, which is taken to be constant according to Ref. [15]. The parameter $\varphi(\theta)$ is determined by

the contact angle θ between cluster and substrate [15], which cannot be directly measured from the TEM images. However, the parameter φ(θ) derived on the basis of surface-diffusion theory is used to express the Pt-cluster volume given by $V(R) = \frac{4\pi}{3} R^3 \varphi(\theta)$. For a known cluster shape, one can calculate the cluster volume and the corresponding value of φ(θ). HRTEM images (Figs. 7(a,b)) show that Pt clusters occur in *fcc* cuboctahedral structure. The volume of clusters with this geometry can be calculated and yields φ(θ)=0.56. The density of surface sites on fcc cuboctrahedral Pt clusters is $n_0=1.3\cdot10^{19}$ m^{-2}. With these data, the D_s' values can be derived. The increase of D_s' from $(1.23\pm0.24)\cdot10^{-23}$ m^2s^{-1} at 200°C to $(4.26\pm0.85)\cdot10^{-22}$ m^2s^{-1} at 300°C suggests a rapid increase of the OR kinetics within this temperature interval. Moreover, an activation energy E_d for the surface diffusion of Pt atoms on a-C substrates of $E_d=0.85\pm0.09$ eV/atom is determined (Fig. 7(c)) assuming an Arrhenius-type dependence for the surface-mass-transport diffusion coefficient $D_s' = D_0 \exp\left(-\frac{E_d}{k_B T}\right)$ with the pre-exponential factor D_0.

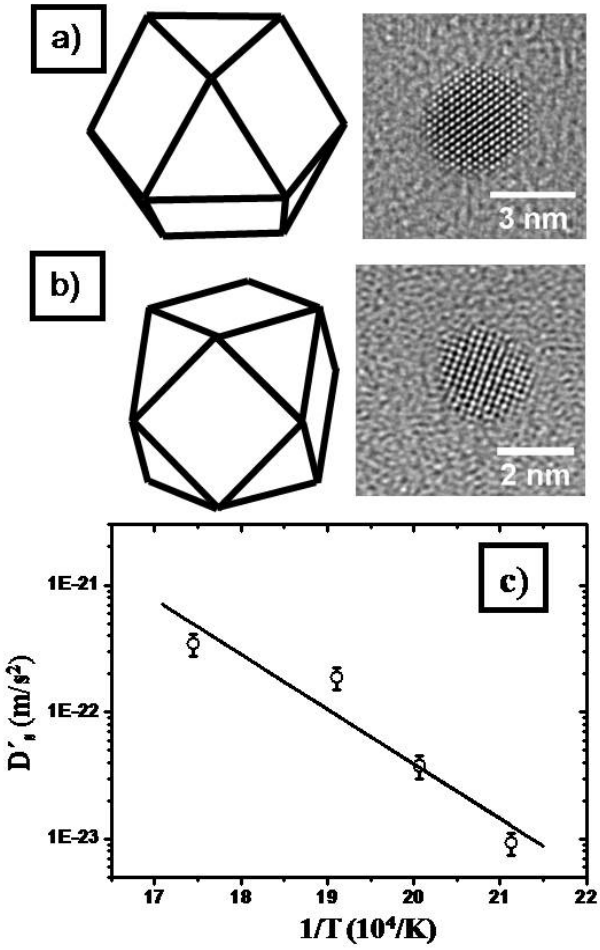

FIG. 7 a) and b) Pt clusters with fcc cuboctahedral structure in the [110]- and [100]-zone axis, respectively: schematic view and the corresponding TEM image; c) Surface-mass-transport diffusion coefficient D_s' as a function of 1/T, which yields an activation energy for the surface diffusion of Pt atoms on a-C substrate of $E_d=0.85$ eV/atom (see the text).

4. Structure of novel nanoparticles

Nanorods, nanowires, and nanotubes have become intensively studied objects in recent years. In contrast, comparably little is known about hollow nanoparticles. Different hollow particles were realized on the mesoscale (diameter >100 nm), but on the nanoscale (diameter <100 nm), only a limited selection of oxide, sulfide, and metal hollow particles is available yet. The group of C. Feldmann (project C1.4.) has focused on synthesizing hollow nanoparticles by the microemulsion approach. These particles were characterized by HRTEM in project C4.5. In the following we show only a few results on recently synthesized hollow nanoparticles. In addition, we have developed a new formalism which allows to derive the true outer (average) diameter and wall thickness of hollow nanoparticles on the basis of XRD patterns. Standard formalisms can only be applied for massive nanoparticles. The validity of the formalism is tested by comparison with HRTEM and dynamic light scattering (DLS) data.

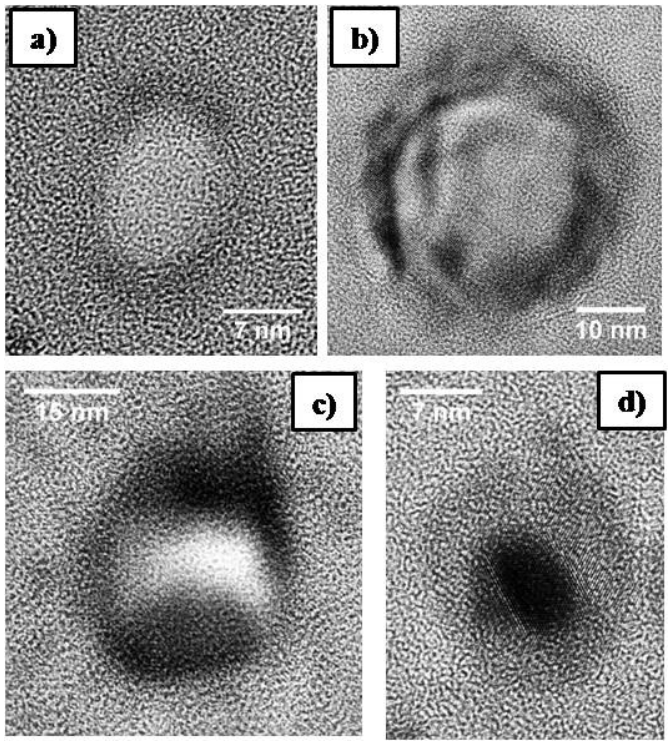

FIG. 8 HRTEM images of (a) Ag, (b) $La(OH)_3$ and (c) CuS hollow clusters; (d) HRTEM image of In-Ag core-shell cluster.

The structure of hollow clusters consisting of Au [5], $La(OH)_3$[6], Ag [7], TiO_2 [8], CuS, $CuS_{1.8}$, CuS_2 [9] and ZnO was studied by HRTEM. The cavity size and crystallinity of the hollow clusters were determined by HRTEM. The ring-like contrast features observed in the HRTEM images Figs. 8(a-c) corresponds to the two-dimensional projection of hollow clusters on the image plane. We note that hollow clusters are sensitive towards irradiation with high-energy electron and tend to collapse already after short illumination duration. Measurements of the wall thickness may therefore not reflect the original wall thickness after synthesis. Fig. 8(d) shows the HRTEM image of a spherical In-Ag core-shell cluster with an In core with a diameter of about 120 Å (the dark region in the center of cluster) and an external Ag shell with a diameter of ~195 Å (ring-like feature surrounding the core). Lattice fringes observed in the cluster walls indicate monocrystalline cluster walls. Most clusters have spherical or oval shapes with asymmetrical lognormal size distributions [10].

With different massive and hollow nanoparticle ensembles available, we have carried out a methodical study which compares the average diameters derived from different techniques (XRD, DLS and TEM) [10]. Depending on the analysis technique, different cluster sizes are obtained from the same (hollow) nanoparticle ensemble. A new formalism was developed which allows the derivation of the inner and outer diameters of hollow clusters from XRD data which is not possible by standard formalism for massive nanoparticles.

XRD yields the volume-averaged size crystallite D_V, which does not correspond to the real average cluster diameter $\overline{D}$, and the average microstrain $\left\langle \varepsilon^2 \right\rangle^{1/2}$. To extract these data from the XRD patterns, the position and integral breadth β of each Bragg reflection are determined after subtracting the background by fitting a Voigt function to the line profile. The corrected lattice parameters of the cluster materials are determined from the XRD line positions by a Cohen-Wagner extrapolation procedure [18] and are given in Table 1. D_V and $\left\langle \varepsilon^2 \right\rangle^{1/2}$ can be in principle determined by using the integral breadth method in the line broadening analysis [19]. However, the lack of experimental data for at least two orders of reflections prevents the determination of D_V and $\left\langle \varepsilon^2 \right\rangle^{1/2}$ by the multiple-line analysis for many nanoparticle ensembles. Instead, the separation of the contributions to the integral breadth induced by the small crystallite sizes and microstrain is carried out within the average-size and strain approximation assuming Cauchy size-broadening and Gauss strain-broadening profiles

$$\beta = \frac{1}{D_V} + \left(\frac{5}{2}\left\langle \varepsilon^2 \right\rangle^{1/2}\right)^2 \frac{k^2}{\beta} \quad \text{for } \beta \text{ in reciprocal units of } k = \frac{1}{d} = \frac{2\sin\theta}{\lambda} \qquad \textbf{(1)}$$

(θ is the Bragg angle and λ is the radiation wavelength) by plotting $(\beta/k)^2$ as a function of β/k^2 according to Refs. [20] as shown in Fig. 9. From the slope $m = 1/D_V$ of this graph the volume-averaged crystallite size can be calculated, while the average microstrain is proportional to its intercept

$$n = \left(5\left\langle \varepsilon^2 \right\rangle^{1/2} / 2\right)^2$$

(see Table 1).

The real average (outer) size $\overline{D}$ can be derived from D_V according to Eq. (2) for ***spherical massive clusters*** with monocrystalline structure and lognormal cluster-size distribution with a distribution dispersion σ_R:

$$D_V = \frac{3}{4}\overline{D}\left(1 + \frac{4\sigma_R^2}{\overline{D}^2}\right)^3 \qquad \textbf{(2)}$$

This expression has to be modified for hollow clusters with an average outer size $\overline{D} = 2\overline{R}$ and cavity radius $\overline{R}_i = \overline{R} - g$ (g: average wall thickness). To calculate $\overline{R}$ or $\overline{R}_i$ of ***hollow spheres*** with lognormal cluster-size distribution Eq. (3) is suggested [10]:

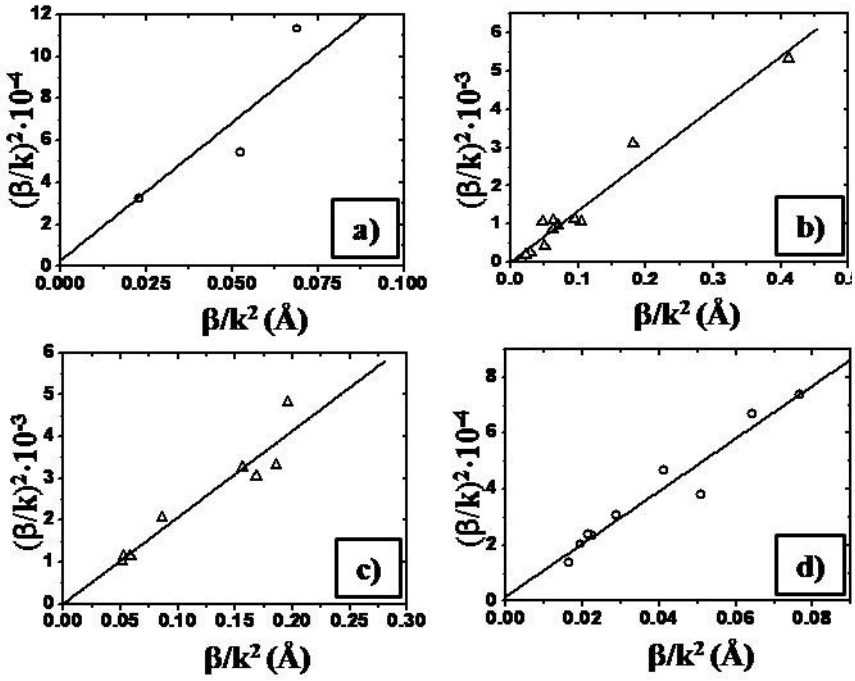

FIG. 9 Plots of $(\beta/k)^2$ as a function of β/k^2 for Ag (a), La(OH)$_3$ (b), CuS (d) and ZnO (d) hollow clusters, respectively.

$$D_V = 2\frac{\int_0^{2\pi}\int_0^{\pi}\int_{\overline{R}_i}^{\overline{R}} (r - \overline{R}_i) r^2 \sin\theta \, d\varphi \, d\theta \, dr}{\int_0^{2\pi}\int_0^{\pi}\int_0^{\overline{R}} r^2 \sin\theta \, d\varphi \, d\theta \, dr}\left(1 + \frac{\sigma_R^2}{\overline{R}^2}\right)^3 = 2\frac{g^2\left(6\overline{R}^2 - 4\overline{R}g + g^2\right)}{4\overline{R}^3}\left(1 + \frac{\sigma_R^2}{\overline{R}^2}\right)^3 \qquad \textbf{(3)}$$

We note that Eq. (3) becomes equal to Eq. (2) for massive clusters described by $g = \overline{R}$ ($\overline{R}_i = 0$). The calculated values for $\overline{D}$ in Table 1 agree well with the average cluster diameters determined by DLS denoted by $\overline{D}_{DLS}$ for Ag, CuS and three La(OH)$_3$ samples which verifies the validity of Eq. (3) [10].

The same procedure is applied to determine the average wall thickness g=37±3 Å and inner radius $\overline{R}_i = 75 \pm 3$ Å for spherical mono-crystalline CuS (covellite) hollow clusters with lognormal size distribution from XRD data analysis [10]. However, the calculated g value is smaller than the average wall thickness g=52±6 Å determined by HRTEM. The difference is assumed to be related to the rather imprecise determination of the wall thickness on the basis of HRTEM images, because the hollow clusters tend to collapse due to illumination with an high-energy electron beam.

Furthermore, the properties of In-Ag core-shell clusters were investigated, which consist of a massive In core surrounded by an Ag shell [10]. The XRD pattern shows three Bragg reflections of Ag, but only the most intense (101) reflection of In. The absence of other diffraction lines in the XRD pattern suggests that InAg alloy were not formed. The properties of the In core could not be further analyzed on the basis of only one reflection. For spherical mono-crystalline Ag shells with a lognormal size distribution, the XRD line broadening analysis results in an average shell thickness g=26±3 Å and consequently an average inner shell radius of $\overline{R}_i = 62 \pm 3$ Å [10]. The g value estimated from XRD is in agreement with g=30±4 Å obtained by HRTEM, demonstrating that the ring with low contrast observed on HRTEM images of In-Ag core-shell clusters indeed represents the Ag shell [10].

Table 1:

Probe	Lattice parameter(s) (Å)	D_V (Å)	$\langle \varepsilon^2 \rangle^{1/2} \cdot 10^{-3}$	$\overline{D}$ (Å)	$\overline{D}_{DLS}$ (Å)
Ag (*massive*)	a=4.084±0.001	253	0.2053	203±17	199
Ag (*hollow*)	a=4.082±0.003	76	2.198	198±32	209
$La(OH)_3$ (*hollow*) (sample 1)	a=6.458±0.008 c=3.848±0.005	75	1.909	96±14	96
$La(OH)_3$ (*hollow*) (sample 2)	a=6.498±0.007 c=3.846±0.004	60	1.349	218±31	225
$La(OH)_3$ (*hollow*) (sample 3)	a=6.493±0.009 c=3.850±0.005	74	0.4601	277±34	284
CuS (*hollow*)	a=3.800±0.005 c=16.356±0.023	48	1.412	-	225
ZnO (*hollow*)	a=3.259±0.002 c=5.218±0.003	106	1.675	70±9	107 *
Core-shell In-Ag only for Ag shell	a=4.090±0.006	66	2.524	-	176 **

* $\overline{D}_{DS}$ *derived by DS after adding a stabilizer substance, which forms an external shell around ZnO HC;*

** $\overline{D}_{TEM}$ *determined by TEM.*

Finally, XRD, HRTEM and differential sedimentation (DS) are used to determine the properties of ZnO hollow clusters, which agglomerate rapidly. To prevent cluster agglomeration, a hydrophilic shell formed by TMP molecules is chemically bonded to their surface. This prevents size determination by DS, due to the unknown thickness of the TMP shell. However, XRD is suited to determine $\overline{D}$ (see Table 1), because the external organic shell contributes only weakly to the XRD pattern. Moreover, comparing the $\overline{D}$ values derived by XRD and DS, the thickness of the external shell can be calculated according to $\overline{R}_{DS} = \overline{R}_{XRD} + g_e$ which yields g_e=18±5 Å [10].

References

- own work with complete titles -

[1] R. Popescu, E. Müller, D.Gerthsen, M. Wanner, M. Schowalter, A. Rosenauer, A. Böttcher, D. Löffler, P. Weis, *Increase of the mean inner Coulomb potential in Au clusters induced by surface tension and its implication for electron scattering*, Phys. Rev. B **76**, 235411 (2007).

[2] R. Popescu, R. Schneider, D. Gerthsen, A. Boettcher, D. Loeffler, P. Weis, M.M. Kappes, *Coarsening of mass-selected Au clusters on amorphous carbon at room temperature*, Surf. Sci. **603**, 3119 (2009).
[3] E. Prestat, R. Popescu, R. Schneider, H. Blank, D. Gerthsen, *Coarsening of Pt clusters on amorphous carbon substrate*, will be submitted to Surf. Sci. (2010).
[4] B. Gamm, R. Popescu, H. Blank, R. Schneider, D. Gerthsen, A. Beyer, A. Gölzhäuser, *Quantitative High-Resolution Transmission Electron Microscopy of Single Platinum Atoms*, submitted to Phys. Rev. Lett. (2010).
[5] C. Zimmermann, C. Feldmann, M. Wanner and D. Gerthsen, *Nanoscale Gold Hollow Spheres Through a Microemulsion Approach*, Small **3**, 1347 (2007).
[6] P. Leidinger, R. Popescu, D. Gerthsen, C. Feldmann, *Nanoscale $La(OH)_3$ Hollow Spheres and Fine-Tuning of Its Outer Diameter and Cavity Size*, Small **6(17)**, 1886 (2010).
[7] C. Kind, R. Popescu, E. Müller, D. Gerthsen, and C. Feldmann, *Microemulsion-based synthesis of nanoscaled silver hollow spheres and direct comparison with massive particles of similar size*, Nanoscale **2**, 2223 (2010).
[8] C. Zurmühl, R. Popescu, D. Gerthsen and C. Feldmann, *Microemulsion-based Synthesis of Nanoscale TiO_2 Hollow Spheres*, submitted to Nanoscale (2010).
[9] P. Leidinger, R. Popescu, D. Gerthsen, H. Lünsdorf, C. Feldmann, *Nanoscale Copper Sulfide Hollow Spheres with precisely adjusted Phase Composition: Covellite (CuS), Digenite ($Cu_{1.8}S$), Chalcocite (Cu_2S)*, submitted to Small (2010).
[10] R. Popescu, P. Leidinger, C. Kind, C. Feldmann, D. Gerthsen, *The structure of lognormal distributions of single-crystalline spherical nanoclusters*, submitted to J. Appl. Cryst. (2010).
[11] C. Kisielowski et al., Micorsc. Microanal., **14**, 469 (2008).
[12] C.T. Nottbohm et al., Ultramicroscopy **108**, 885 (2008).
[13] A. Weickenmeier and H. Kohl, Acta Cryst., **47**, 590 (1991).
[14] P. A. Doyle and P. S. Turner, Acta Cryst., **24**, 390 (1968).
[15] B. K. Chakraverty, J. Phys. Chem. Solids **28**, 2401 (1967).
[16] M. Zinke-Allmang, L. C. Feldman and M. H. Grabow, Surf. Sci. **16(8)**, 377 (1992).
[17] M. McLean and H. Mykura, Surf. Sci. **5**, 466 (1966).
[18] C. N. J. Wagner, "*Local Atomic Arrangements Studied by X-Ray Diffraction*", Eds. J. B. Cohen and J. E. Willard, Gordon and Breach, New York, 1966.
[19] J.I. Lagford, R. Delhez, Th. H. de Keijser and E. J. Mittemeijer, Aust. J. Phys. **41**, 173 (1988).
[20] J. I. Langford, "*Accuracy in Powder Diffraction II, NIST Special Publication No. 846"*, Eds. E. Prince and J.K. Stalick, Gaithersburg, MA, US Department of Commerce, pp. 110-126 (1992).